A prototype of pCT scanner: first tests

J. A. Briz[1], I. Posadillo[1], V.G. Távora[1], E. Nácher[2], M.J.G. Borge[1], O. Tengblad[1], A. Perea[1], A. Ortiz[1], J. D. Ovejas[1], and S. Viñals[1,3]
[1]Instituto de Estructura de la Materia, CSIC, Madrid, Spain
[2]Instituto de Física Corpuscular, CSIC-UV, Valencia, Spain
[3]Centro de MicroAnálisis de Materiales (CMAM), UAM, Madrid, Spain
jose.briz@csic.es

***Abstract*—Proton therapy technique for cancer treatment offers a high selectivity with respect to conventional radiotherapy with X- and γ- rays due to the properties of the interaction of protons with matter. Very accurate and precise treatment plans and a good control on the dose deposition are required to exploit the full potential of the technique. The substitution of the currently used X-ray Computed Tomography (xCT) by proton Computed Tomography (pCT) in the design of treatment plans would allow for a reduction in proton range uncertainties. This would make possible an important improvement in the accuracy and precision of treatment plans. With this aim, a prototype of pCT scanner is under study. It includes two tracking detectors which provide information on the proton trajectories and a residual energy detector to determine the energy loss while traversing the object scanned. A proof-of-concept experiment has been performed using low-energy protons and a simplified prototype with only the two tracking detectors. The results obtained in the measurement are presented and discussed.**

***Keywords* — proton, proton therapy, proton Computed Tomography, particle tracking, silicon detectors, DSSD, scintillators, $LaBr_3$.**

I. Introduction

Cancer is a leading cause of death worldwide and accounted for nearly 10 million deaths in 2020. This motivates the tremendous efforts which are devoted worldwide to improve the diagnostics and treatment techniques and the mitigation of its consequences.

Proton therapy as a tumor treatment technique was first proposed by Robert R. Wilson in 1946 and the first treatments were performed in Berkeley (USA) in 1954 and Uppsala (Sweden) in 1957. Proton therapy offers the great advantage with respect to conventional radiotherapy with X- or γ-rays of being more selective applying a higher dose to the tumor with respect to the surrounding healthy tissues. The reason is that the stopping power of protons increases continuously while slowing down. This causes the deposition of a large fraction of the proton initial kinetic energy in the very last millimeters of its range. The curve describing the behavior of the stopping power vs. depth for heavy-charged particles such as protons shows a narrow peak at the end of its path where most of the energy is lost, which is the so-called Bragg peak.

The fact that the energy deposition occurs in a very reduced region at the end of the proton path requires, at least, two improvements. First, the design of more accurate and precise treatment plans than those of conventional radiotherapy. This is needed to reduce the uncertainties on proton ranges avoiding a high dose to be applied to healthy tissues. Second, a very good control of proton ranges during treatment which can be achieved by means of a reliable and precise system of on-line proton range verification providing information in real time of the location of the deposited dose.

Currently proton therapy treatment plans are designed using images obtained via X-ray Computed Tomography (xCT). The result is a map of Hounsfield Units (HU) which basically provides information on the attenuation coefficient at each location relative to that of water and air. In continuation, to obtain the treatment plan with protons, a conversion to a map of Relative Stopping Powers (RSP), which is the interesting physical quantity in proton therapy, is made. This conversion induces relatively large uncertainties in the range of protons which can be as large as 5% in the abdomen or 11% in the head [1]. Assuming that an optimized imaging system of Computed Tomography directly with protons is developed, these uncertainties could be reduced to below 1% since one directly measures RSP and the conversion from HU would not be needed.

In this context, a prototype of proton Computed Tomography scanner is under study. A typical proton scanner is formed by a tracking system including two detectors placed one before and another after the object to be scanned as it is shown in Fig. 1. Then, a residual energy detector is used to fully stop the protons at the end of the path and be able to determine their energy loss in the object.

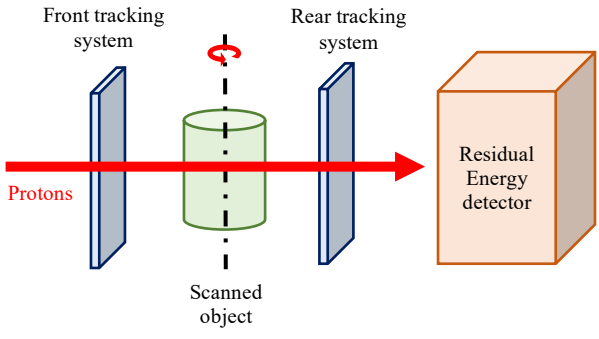

Fig. 1. Schematic structure of a pCT scanner

II. PROTOTYPE OF PCT SCANNER

The prototype to be tested includes two Double-sided Silicon Strip Detectors (DSSDs) placed before and after the object (sample) as tracking detectors. The DSSD detector, described in detail in [2], is formed by 16 horizontal and 16 vertical strips of 3 mm width each which provide an approximate field of view of 50 x 50 mm^2 with 256 pixels of 3x3 mm^2 area each. An array of 2x2 $LaBr_3(Ce)$ crystals is used as residual energy detector, being each of them of 27 x 27 mm^2 and 4-cm-long. The $LaBr_3(Ce)$ crystals are coupled to 6-cm-long $LaCl_3(Ce)$ in "phoswich" configuration as described in [3]. For proton imaging the second layer of $LaCl_3(Ce)$ scintillator is not used as protons of up to 120 MeV are fully stopped in the first layer of $LaBr_3(Ce)$ crystals. This detector was already tested for proton detection showing successful results published in [4].

III. PROOF-OF-CONCEPT EXPERIMENT

A proof-of-concept measurement was performed in 2019 at Centro de MicroAnálisis de Materiales (CMAM) facility in Madrid. The 5-MV Cockcroft-Walton tandem accelerator of CMAM provides protons of up to 10 MeV kinetic energy. As the energy of protons provided was low, the prototype was simplified to two tracking detectors being DSSDs of 60 and 500 µm thickness. In this measurement, the second tracking detector acted both as tracking and residual energy detector at the same time. The experimental chamber used is shown in Fig. 2 and a closer look on the detectors and sample can be seen in Fig. 3. The proton beam was arriving from the left-hand side then impinged on a 1.2 mg/cm^2 bismuth scattering target. The prototype was placed at an angle of 24 degrees with respect to the primary beam incidence direction to both, reduce the beam intensity up to counting rate values below 10 kHz and completely and continuously illuminate the detectors and sample to be scanned. The experimental chamber was kept under a vacuum of approximately $1x10^{-6}$ mbar during the whole experiment.

Three different samples, shown in Fig. 4, were analyzed. They were thin samples due to the low beam energy and were

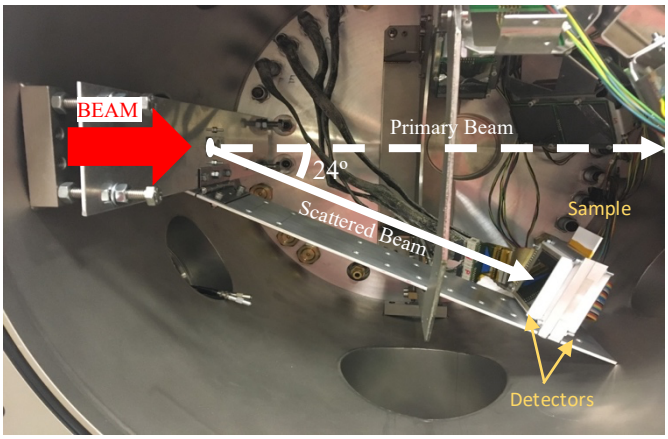

Fig. 2. Experimental setup used at the CMAM facility. The 10-MeV proton beam was scattered at a bismuth target. The detectors and sample were placed at 24º with respect to the primary beam direction. A close-up view on the detectors and sample area is shown in Fig. 3.

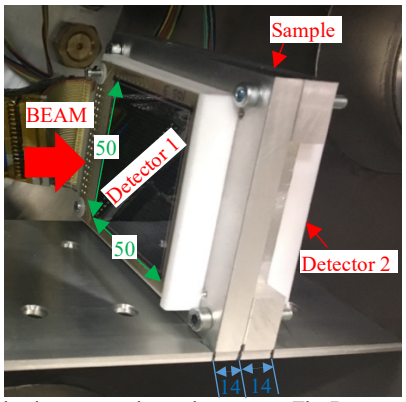

Fig. 3. Image of the detectors and sample support. The Detector 1-sample and sample-Detector 2 distances are indicated in blue. Dimensions are given in mm.

all built on a 500 µm PVC matrix layer. The first sample, shown on the left-hand side, contains a cross pattern made with a 200-µm-thick aluminum layer on top of the PVC layer. The second sample, which can be seen at the center of Fig. 4, contained four different circular regions of 10(1) mm diameter each: one with only a 200-µm-thick aluminum layer (1), another with just a hole (2), a third one containing 200-µm-thick aluminum layer on top of the 500-µm-thick PVC matrix (3) and the last one built with 1-mm-thick aluminum (4). The third sample was built with holes of different diameters and separations emulating a Derenzo pattern. The holes and separations are of 4, 6 and 8 mm organized in three rows as it can be seen in Fig. 4.

The detectors were connected to Mesytec MPR-64 preamplifiers and STM16 amplifiers and their signals were finally digitized by a CAEN ADC V785 VME module integrated in a Multi Instance Data Acquisition System [5]. The data was collected in an event-by-event basis and stored in list mode files.

IV. DATA ANALYSIS

The energy spectra of both Double-sided Silicon Strip detectors were obtained from the list mode data files. The image of the samples was obtained by imposing a time coincidence condition between both DSSD detectors and that only one vertical and one horizontal strip were hit with similar energy. Then, the pixel corresponding to the proton hit in each detector was determined as the crossing between the horizontal and vertical strips activated. The image was built by determining the crossing position of the trajectory of the protons with the sample plane, also known as image plane. The trajectory of protons was assumed to be a line connecting the pixels hit in each detector. Since both detectors were placed exactly at the same distance from the sample, 14 mm as shown in Fig. 3, the XY coordinates at the image plane were obtained just by arithmetic average of the coordinates at each detector.

The statistics accumulated was not the same in every pixel. The reason for that is the Rutherford scattering occurring at the bismuth target. Consequently, the detector hit map as well as the image showed an intensity gradient following the conical symmetry of the scattered-protons distribution. As a result, higher statistics was obtained at pixels closer to the incident

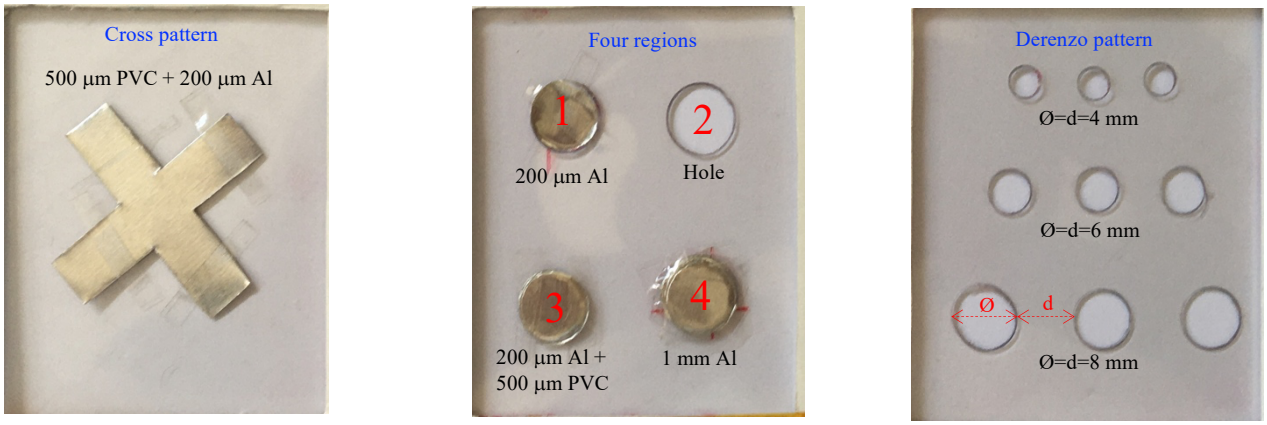

Fig. 4. Set of samples made with a 500-µm PVC matrix layer containing different patterns that were analyzed at the CMAM facility using a 10-MeV-proton beam.

proton beam direction (equivalent to 0º deviation angle) decreasing as one moves towards larger deflection angles.

Having a look at the experimental setup shown in Fig. 2, one can see that the upper part of both detectors is closer to 0 degrees and, therefore, accumulates larger statistics. To correct for this effect, the summed energy in each pixel is normalized by the number of hits detected. In this way, the average energy deposited per detected proton at each pixel is obtained.

V. RESULTS

The images shown in Fig. 5 were obtained from the samples shown in Fig. 4. Remarkable similarities between the images and the real samples are observed. A nice uniformity of the PVC matrix region can be seen in the three images with a value of about 3200 keV. A slight vertical distortion can be seen in the three images corresponding to X = 30 mm caused by a dead strip in the frontal DSSD detector.

A. Sample with cross pattern

A picture of the sample containing the cross pattern is shown on the left-hand side of Fig. 4. It was built by placing a 200 µm aluminum layer on top of the 500-µm-thick layer of PVC. The corresponding image obtained in the experiment is shown at the same side in Fig. 5. The cross pattern can be seen in red including a penumbra region shown in yellow. The uniform PVC background is seen with an energy loss of the protons of about 3200 keV (in green), meanwhile the region of aluminum + PVC of the cross is observed with 6500 keV approximately (in red) and the region of penumbra with about 5500 keV (in yellow). A detail showing the sensitivity of our device can be highlighted by the two more intense red regions indicated with two white circles. They correspond to the thin cellophane tape layers of about 20 µm thickness used to stick the cross pattern to the PVC matrix. The length and width of cross arms were determined in the projection of a slice chosen in the region of interest. Then a fit to a generalized gaussian function, i.e. $f(x) = \frac{A}{\sqrt{2\pi}\sigma} e^{-\frac{1}{2}\left(\frac{|x-\mu|}{\sigma}\right)^n}$ was performed, where n=4 order was chosen for the arm width and n=10 for the arm length. The FWHM of the 1D distributions was obtained using the expression $FWHM = 2 \cdot \sigma \cdot (2 \cdot \log(2))^{1/n}$. The length and width of the two cross arms were determined as the average of the FWHMs. The resulting values are compared to the real dimensions of the sample in Table I. The results agree within the error bars with the real dimensions of the sample.

B. Sample with four regions

The sample with four different regions is shown in the central

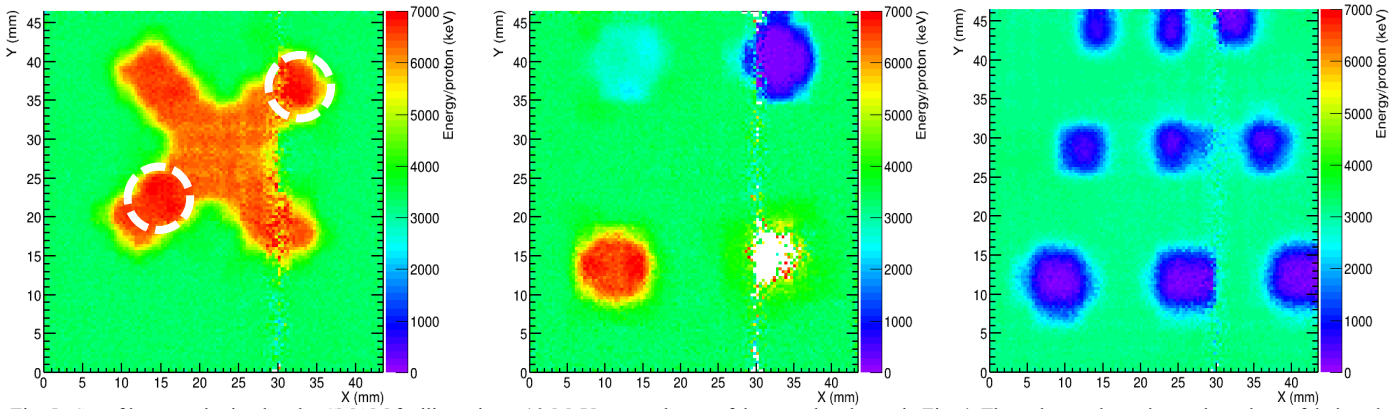

Fig. 5. Set of images obtained at the CMAM facility using a 10-MeV-proton beam of the samples shown in Fig. 4. The colour palette shows the values of deduced energy lost in the sample. The cross-pattern sample is shown on the left, the sample with four regions in the middle and the one with Derenzo pattern on the right side. The sample with cross pattern has indicated two regions which appear in red in the image which correspond to thin cellophane-tape layers of ~20 µm that can be seen in the picture of Fig. 4 and that our system was able to detect.

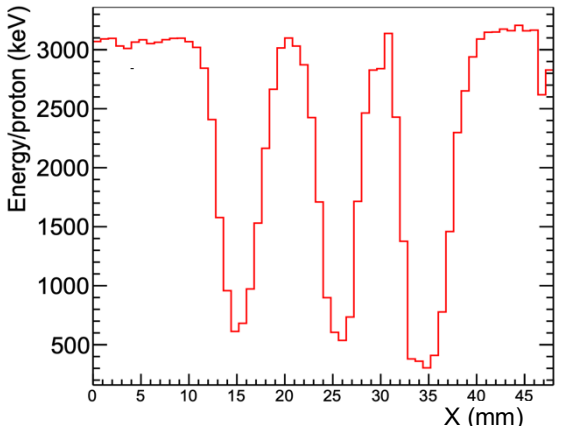

Fig. 6. One-dimensional horizontal projection obtained from the central slice of pixels for the row with 4-mm-diameter holes in the image of the sample with Derenzo pattern shown on the right-hand side of Fig. 5.

part of Fig. 4. The corresponding image is shown in the central part of Fig. 5. The uniform PVC background is found to be of similar value of energy loss than in the previous sample. The region 1 shows a value of proton energy loss of about 2500 keV meanwhile the region 2, as expected, shows a value of 0 keV. The region 3 is obtained with a value of approximately 6500 keV. Protons are stopped in the 1-mm-thick aluminum foil placed in position 4. For this reason, a white color is seen which corresponds to no signal in the back DSSD detector. The values estimated for the diameter of the three regions with data (empty hole, 200-μm Al and region with 200-μm Al + 500 μm PVC) are given in Table I. The real diameter, as already mentioned, was 10(1) mm. It is very encouraging to see that the values obtained are consistent with the real sample.

TABLE I
PROPERTIES OF THE IMAGES OBTAINED

SAMPLE WITH DERENZO PATTERN		SAMPLE WITH CROSS PATTERN			SAMPLE WITH FOUR REGIONS		
Sample hole diameter (mm)	Image hole diameter (mm)		Sample size (mm)	Image size (mm)	Region	Sample region diameter (mm)	Image region diameter (mm)
4(1)	4.1(2)	Arm length	35(1)	35.9(2)	1	10(1)	11(2)
6(1)	6.5(3)	Arm width	8(1)	7.9(2)	2	10(1)	10.1(8)
8(1)	7.5(2)				3	10(1)	10.1(15)

Dimensions of the holes in the sample with Derenzo pattern, arms of the sample with cross pattern and diameter of 3 regions in the sample with four regions obtained from the images as compared to real values. The dimensions are obtained in the images as the Full Width at Half-Maximum (FWHM) from the 1D horizontal projections of slices at the regions of interest.

C. Sample with Derenzo pattern

A sample with a Derenzo pattern was used for the evaluation of the spatial resolution. It is shown in the right-hand side picture of Fig. 4. The corresponding image can be seen at the same side of Fig. 5. To study the size of the holes obtained in the image, a one-dimensional spectrum was obtained by selecting a slice formed by the central line of pixels corresponding to each row of holes. This result can be seen in Fig. 6 for the case of the 4-mm diameter holes as an example. Each hole in the sample is seen as an inverted gaussian. A gaussian fit was performed and an average of the obtained FWHM values allowed to estimate the hole dimensions. The resulting values are given on the left-hand side of Table I. A good agreement is found between the real sizes of the holes and the ones determined from the image.

VI. DISCUSSION

The results obtained for the three samples studied are promising. For the sample with cross pattern, the dimensions obtained for the arm length and width agree within the error bars with the real dimensions. In addition, the PVC background shows a good uniformity. The device has sensitivity for thin layers as the presence of cellophane tape was identified in the image, see Fig. 5. The results for the sample with four regions showed that different thicknesses and materials are well identified and that the measured diameters for the three holes evaluated agree nicely with the values of the real sample. The study of the sample with the Derenzo pattern demonstrated that our device has better spatial resolution than 4 mm. In addition, the diameters of the 4-, 6- and 8-mm holes were well determined from the image.

VII. CONCLUSIONS

Proton therapy has an enormous potential for cancer treatment however improvements in treatment plans and dose verification are required to fully exploit its capabilities. With this purpose, our collaboration is working in the development of a proton Computed Tomography scanner.

In the present article, the results of a proof-of-concept experiment performed at the Centro de MicroAnálisis de Materiales facility in Madrid are presented. A simplified version of our prototype is adopted due to the low energy of the proton beam. Direct images were obtained for different thin samples. The properties of those images are presented and discussed in this contribution. In general, satisfactory results were obtained reproducing nicely the samples analyzed.

The results presented here constitute the first step in the development of our prototype that should be tested under more realistic conditions. With this aim, a new measurement was proposed to perform tomography scans of 3D objects with 100 MeV proton beams. The experiment has been performed in June 2021 and the data analysis is currently on-going.

ACKNOWLEDGMENT

Authors want to thank the CMAM (Madrid) staff for their contribution in the performance of the measurement. This work has been supported by the PRONTO-CM B2017/BMD-3888 project funded by Comunidad de Madrid (Spain).

REFERENCES

[1] Robert P Johnson, Rep. Prog. Phys. 81, (2018) 016701.
[2] O. Tengblad *et al*., Nuclear Instruments and Methods in Physics Research A 525, (2004) 458–464.
[3] O. Tengblad *et al.*, Nuclear Instruments and Methods in Physics Research A 704, (2013) 19–26.
[4] E. Nácher *et al.*, Nuclear Instruments and Methods in Physics Research A 769 (2015) 105–111.
[5] Multi Instance Data Acquisition System. http://npg.dl.ac.uk/MIDAS/